



Physical and optical characteristics of heavily melted “rotten” Arctic sea ice

Carie M. Frantz^{1,2}, Bonnie Light¹, Samuel M. Farley¹, Shelly Carpenter¹, Ross Lieblappen^{3,4},
Zoe Courville⁴, Mónica V. Orellana^{1,5}, and Karen Junge¹

¹Polar Science Center, Applied Physics Laboratory, University of Washington, Seattle, Washington, 98105 USA

²Department of Geosciences, Weber State University, Ogden, Utah, 84403 USA

³Vermont Technical College, Randolph, VT, 05061 USA

⁴US Army Engineer Research Development Center - Cold Regions Research and Engineering Laboratory, Hanover, New Hampshire, 39180 USA

⁵Institute for Systems Biology, Seattle, Washington, 98109 USA

Correspondence to: Bonnie Light (bonnie@apl.washington.edu)

1 **Abstract.** Field investigations of the properties of heavily melted “rotten” Arctic sea ice were carried out on shorefast and drifting
2 ice off the coast of Utqiaġvik (formerly Barrow), Alaska during the melt season. While no formal criteria exist to qualify when ice
3 becomes “rotten”, the objective of this study was to sample melting ice at the point where its structural and optical properties are
4 sufficiently advanced beyond the peak of the summer season. Baseline data on the physical (temperature, salinity, density,
5 microstructure) and optical (light scattering) properties of shorefast ice were recorded in May and June 2015. In July of both 2015
6 and 2017, small boats were used to access drifting “rotten” ice within ~32 km of Utqiaġvik. Measurements showed that pore space
7 increased as ice temperature increased (-8 °C to 0 °C), ice salinity decreased (10 ppt to 0 ppt), and bulk density decreased (0.9 g
8 cm⁻³ to 0.6 g cm⁻³). Changes in pore space were characterized with thin-section microphotography and X-ray micro-computed
9 tomography in the laboratory. These analyses yielded changes in average brine inclusion number density (which decreased from
10 32 mm⁻³ to 0.01 mm⁻³), mean pore size (which increased from 80 μm to 3 mm) as well as total porosity (increased from 0% to >
11 45%) and structural anisotropy (variable, with values generally less than 0.7). Additionally, light scattering coefficients of the ice
12 increased from approximately 0.06 cm⁻¹ to > 0.35 cm⁻¹ as the ice melt progressed. Together, these findings indicate that Arctic sea
13 ice at the end of melt season is physically different from the often-studied summertime ice. If such rotten ice were to become more
14 prevalent in a warmer Arctic, this could have implications for the exchange of fluid and heat at the ocean surface.



1 Introduction

15 There exists a fairly predictable annual evolution for the Arctic seasonal sea ice cover: winter, snow melt, pond formation, pond
16 drainage, rotten ice [DeAbreu *et al.*, 2001]. Considerable attention has been given to characterization of these various states and
17 their transitions. *In situ* observations during the summer melt season are typically straightforward through the pond drainage stage,
18 but, as ice conditions deteriorate, it becomes increasingly difficult to work on or around the most fragile state, rotten ice. During
19 the summer of 1894, Nansen, in his seminal work *Farthest North* (1897, p. 433) described it well, “Everything is in a state of
20 disintegration, and one’s foothold gives way at every step.” Barber *et al.* [2009] encountered extensive rotten ice in the Beaufort
21 Sea pack in September 2009, where they found an ice cover that was composed of small remnants of decayed and drained ice
22 floes interspersed with new ice. The remotely sensed radiometric characteristics of this ice cover appeared indistinguishable from
23 old, thick multiyear ice. But such characterization is largely indicative of the physical properties of the ice on meter to decameter
24 scales, leaving the microstructural properties of ice as it experiences extreme summer melt largely undocumented.

25 The relatively high temperatures and abundant sunlight of summer cause sea ice to “rot”. While the microstructure of winter ice is
26 characterized by small, isolated brine inclusions, with brine convection restricted to the lower reaches of the ice, and spring ice is
27 characterized by increased permeability and brine convection through the full depth of the ice cover [Jardon *et al.*, 2013; Zhou *et al.*
28 *et al.*, 2013], the defining characteristics of rotten ice may be its high porosity and enhanced permeability. Warming causes changes
29 in the ice structure including enlarged and merged brine and gas inclusions (see, e.g., Weeks and Ackley, 1986; Light *et al.*, 2003).
30 Columnar ice permeability increases drastically for fluid transport when the brine volume fraction exceeds approximately 5%
31 [Golden *et al.*, 2007; Pringle *et al.*, 2009]. In a previous study on shorefast ice, brine volume fractions were found to exceed this
32 5% threshold for permeability through the entire depth of the ice from early May onwards [Zhou *et al.*, 2013].

33 In general, the connectivity of an ice cover is known to contribute to ocean-atmosphere heat transfer [Weeks and Ackley, 1986;
34 Hudier *et al.*, 1995; Lytle and Ackley, 1996; Weeks, 1998; Eicken *et al.*, 2002], exchange of dissolved and particulate matter
35 [Freitag, 1999; Krembs *et al.*, 2000], including nutrients [Fritsen *et al.*, 1994], salinity evolution of the ice cover [Untersteiner,
36 1968; Wettlaufer *et al.*, 2000; Vancoppenolle *et al.*, 2007], and surface melt pond distribution [Eicken *et al.*, 2002]. For rotten ice,
37 permeability is typically large enough to render the ice cover to be in connection with the ocean throughout its depth. As a result,
38 rotten ice may have a very different biogeochemical environment for sea-ice microbial communities than ice with connectivity
39 properties typical of winter, spring, or even early to mid-summer.

40 Increases in ice permeability result in an increase in the amount of surface meltwater that can penetrate through a melting ice
41 cover, both from the top of the ice downwards [e.g., Untersteiner, 1968], as well as from the bottom of the ice upwards [e.g.,
42 Eicken *et al.*, 2002; Jardon *et al.*, 2013]. The convective overturning of meltwater pooled beneath the ice can contribute
43 significantly to enlargement of pores and internal melt. In fact, during the Surface Heat Budget of the Arctic Ocean (SHEBA)



44 field campaign, [Eicken *et al.*, 2002] noted that high advective heat fluxes into the permeable ice found on melt pond bottoms and
45 first-year ice likely contributed to the breakup and disintegration of the ice cover toward the end of the melt season.

46 As a result of the notable connectivity of its microstructure, rotten ice also has reduced structural integrity, which can have
47 implications for ice dynamics. Though it is known to have diminished tensile and flexural strength [Richter-Menge and Jones,
48 1993; Timco and O'Brien, 1994; Timco and Johnston, 2002], such details have not been well-characterized. Measurements by
49 Timco and Johnston [2002] demonstrated that in mid-May, the ice had about 70% of its mid-winter strength. By early June, about
50 50% and by the end of June, 15%–20% of its mid-winter strength. The ice strength during July was only about 10% of midwinter
51 strength. Such changes in strength may be relevant to the late summer behavior of Arctic ice-obligate megafauna. With increasing
52 melt season length [Stroeve *et al.*, 2014], the future could bring increasing areas of rotten ice. Because it represents the very end of
53 summer melt, its presence matters for the longevity of the ice cover. If the ice melts completely, then the open ocean will form
54 new ice in the autumn. Only ice remaining at the end of summer can become second-year, and subsequently, multiyear ice.

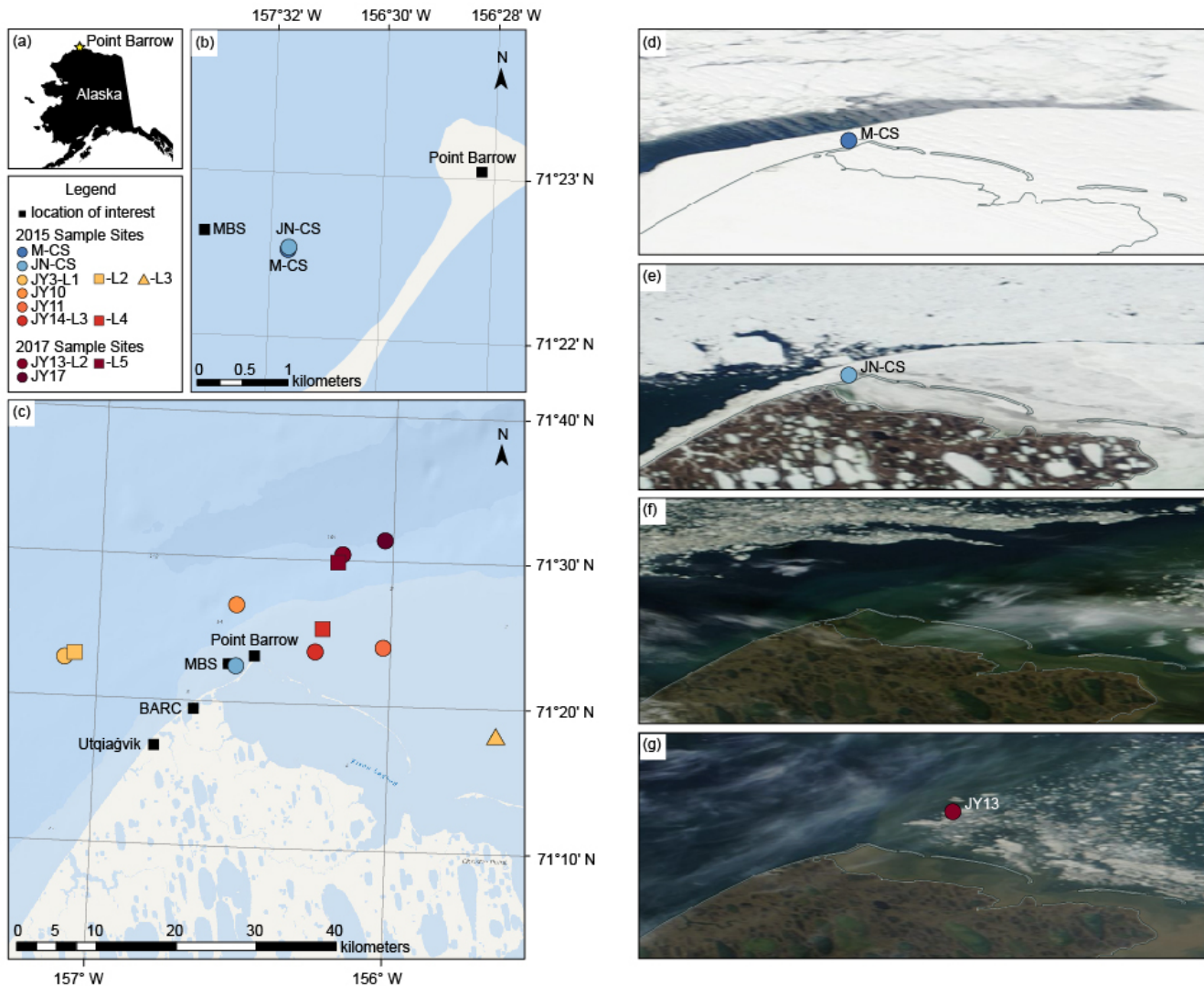
55 To address questions about the physical characteristics of rotten sea ice, a targeted field study was carried out at Utqiagvik
56 (formerly Barrow; 71.2906° N, 156.7886° W), Alaska during May, June, July 2015, with further sample collection carried out in
57 July 2017. The May and June sampling sessions were for the purpose of collecting ice to be used for baseline studies. In July,
58 small boats were used to search for, and sample, rotten ice off the coast.

2 Materials and methods

2.1 Sample collection and description

59 Sea ice samples and field measurements were collected from locations near the north coast of Alaska (Fig. 1-2, Table A1).
60 Samples were collected at three different time points in order to define the progression of melt: May to collect baseline data on the
61 ice properties, June to observe its progression, and July to capture rotten ice (Fig. 3).

62 All ice cores were drilled using a 9-cm diameter Kovacs Mark II corer (Kovacs Enterprise, Roseburg, Oregon, USA) through the
63 full depth of the ice. Extracted cores were photographed and either bagged whole or as 20-cm subsections for subsequent
64 laboratory analysis. At each sampling site, a single core was used for temperature and density profiles. Bagged cores were stored
65 up to several hours in insulated coolers for transport back to the Barrow Arctic Research Center (BARC) laboratory, and
66 immediately placed in one of several walk-in freezers set to -20 °C for archival cores to be saved for later processing, or, for cores
67 processed at BARC, at approximate average *in situ* core temperatures (-5 °C in May, -2 °C in June, -1 °C in July), referred to
68 subsequently in this text as “working” temperatures.



69 Figure 1. Map of sea ice sample collection sites. (a) Point Barrow (star) is the northernmost point in the United States. (b)
 70 Landfast sea ice sample collection sites for May 2015 (M-CS, dark blue) and June 2015 (JN-CS, light blue), shown relative to the
 71 2015 SIZONet Mass Balance Site (MBS) and Point Barrow. M-CS and JN-CS were separated by less than 30 m. (c) Ice sample
 72 collection sites in May 2015 (dark blue), June 2015 (light blue), July 2015 (orange and red), and July 2017 (magenta) relative to
 73 Point Barrow, the 2015 MBS, the Barrow Arctic Research Center (BARC), and the town of Utqiagvik, Alaska, USA. Alaska
 74 Coastline base map provided by the Alaska Department of Natural Resources (1998). ArcGIS Ocean base map sources: Esri,
 75 GEBCO, NOAA, National Geographic, DeLorme, HERE, Geonames.org, and other contributors (2016). (d-g) NASA MODIS
 76 satellite images of Point Barrow on clear-sky days on (d) 7 May 2015, showing the location of the M-CS sample site (dark blue);
 77 (e) 7 June 2015, showing the location of the JN-CS sample site (light blue); (f) 6 July 2015, showing the general locations of
 78 highly mobile ice proximal to Point Barrow; and (g) 13 July 2017, showing the location of the JY-13 sample site (magenta). No
 79 clear-sky images were available for the July 2015 sampling dates (JY3, JY10, JY11, and JY14) or for the 17 July 2017 (JY17).
 80 Satellite imagery retrieved from worldview.earthdata.nasa.gov (2017), coastline overlay © OpenStreetMap contributors, available
 81 under the Open Database License.

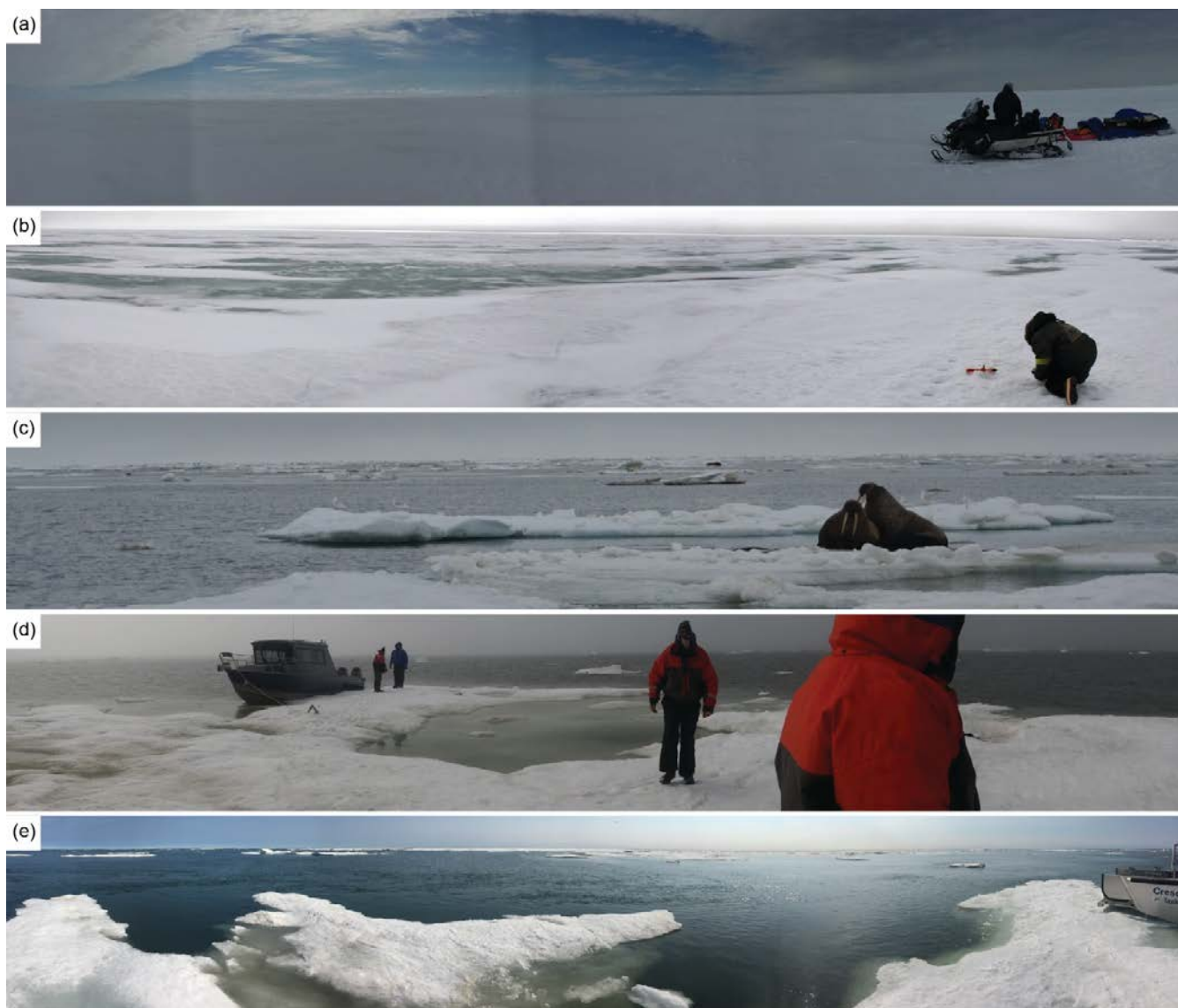


Figure 2. Sea ice in the vicinity of Utqiagvik, Alaska, USA during summer melt. a) Photomosaic of 8 May 2015 sample site. b) Panorama photograph of 7 June 2015 sample site. c) Photograph of a rotten floe from 3 July 2017 (not sampled, but another in the vicinity that was not photographed was). d) Panorama photograph of the floe sampled on 11 July 2015. e) Panorama photograph of a floe sampled on 13 July 2017.



82 Figure 3. Photographs of sampled rotten ice floes. (a) JY3-L3, (b) JY10, (c) JY11, (d) JY14-L3, (e) JY14-L4, (f) JY13-L1, (g)
83 JY13-L2, (h) JY17.

2.1.1 May

84 The first set of samples was collected on 6 May 2015 from landfast, first-year, snow-covered congelation sea ice in a region of
85 undeformed ice 2 km southwest of Point Barrow and ~0.9 km due east of the University of Alaska Fairbanks 2015 SIZONet Sea
86 Ice Mass Balance Site (“MBS”) [Eicken, 2016] (Fig. 1b, GPS coordinates in Table A1). Flat, snow-covered ice with no noticeable
87 ridging was visible for many kilometers in all directions (Fig. 2a). Once cleared of snow (depth of 14–18 cm, -9 °C at 9 cm below
88 the surface), the ice appeared flat and uniform. Snow was cleared prior to the collection of samples. The measured ice thickness
89 ranged from 141–150 cm at the sampling site, which is substantially thicker than the 105 cm thickness reported at the nearby
90 MBS. The uppermost ~10 cm (7%) of the ice was above freeboard. At the time of our sampling, the altimeter at the MBS had
91 failed, so ice thickness was estimated from the thermistor string and was considered to have large uncertainty. Ambient air
92 temperature on the date of sampling was -9 °C at 11:00 AM. Samples collected for analysis were subsectioned in the field at
93 depths of 0-20 cm (top horizon), 32-52 cm (middle horizon), and the bottom 20 cm of each core (bottom horizon).



2.1.2 June

94 The second set of samples was collected on 3 June 2015 from within 30 m of the site sampled in May (Fig. 1b). The ice had begun
95 to form melt ponds (Fig. 2b), which we avoided during sampling. The June ice had thickness ranging from 149–159 cm, with ~21
96 cm above freeboard (14 %). It is likely that some of the increased ice thickness observed, compared to what was measured in
97 May, was due to the addition of retextured snow at the surface following a significant rain event during the last week of May
98 (SIZONet, 2017, observations for Utqiagvik by Billy Adams, <https://eloka-arctic.org/sizonet/>), which manifested as a layer of
99 granular ice. Ambient air temperature on the date of sampling was -1.6 °C at 12:00 PM. Samples collected for analysis were
100 subsectioned in the field at depths of 0–20 cm (top horizon), 45–65 cm (middle horizon), and the bottom 20 cm of each core
101 (bottom horizon).

2.1.3 July 2015

102 In 2015, the landfast ice broke away from the local coastline during the third week of June (Fig. 1f). July samples were drilled
103 from isolated floes accessed by small boats within a radius of 32 km from Point Barrow (Fig. 1c). Floes in July varied greatly in
104 size, thickness, and character.

105 On 3 July 2015, the sea was ice-free within an ~8 km radius of Pt. Barrow; beyond this were regions of mixed ice, with both
106 sediment-rich and sediment-poor floes. Ice encountered near the barrier islands bounding Elson Lagoon included many apparently
107 grounded floes as well as some small (~7 m above freeboard), blue icebergs. Wildlife was abundant in the region, with king and
108 common eider, walrus, bearded seals, a grey whale, and a large pod of ~100 beluga whales observed. Cores were drilled in three
109 different floes: a thick (170 cm) “clean” floe (JY3-L1; with naming convention month (M, JN, JY), day of month – location
110 number), a small (~2 m², 86–150 cm thick in the center) sediment-rich floe (JY3-L2), and a large, heavily-ponded floe (JY3-L3;
111 the single core collected from this floe measured 145 cm long). At all sites, freeboard depth was difficult to determine due to the
112 high variability in the underside of the ice, however, roughly 10–12% of ice cored was above freeboard. Other than the variable
113 thickness of the floes and high sediment content in some floes, the character of the ice was similar to what was observed in June.

114 Cores collected on 10 July 2015 (JY10) came from a sediment-rich, heavily-ponded floe with an ice thickness measured in a non-
115 ponded part of the floe of 190 cm. Ice in non-ponded areas was solid and saline, similar to what was observed in June and on 3
116 July. Cores from ponded areas of the floe (collected from ponds ~18 cm deep) were visibly highly porous (rotten) and ranged
117 from 58–90 cm thick. During the course of two hours of sample collection, the floe began to break up under light wave action
118 (winds in the region increased from ~10 to 15 knots during the course of sample collection), forcing our team to retreat to the boat.
119 In one case, a crack developed that connected core holes drilled across a ponded area; in another, a large crack developed across
120 the width of the floe.



121 On 11 July 2015, additional cores (64–90 cm length) were sampled from a ponded area of a clean (sediment-poor) floe of rotten
122 ice (JY11). As with the 10 July floe, ice in non-ponded areas was solid and saline, partially drained but not heavily rotted. The
123 upper portion of the ice was pitted and drained. Ice beneath melt ponds (cores collected were submerged under 9–15 cm water)
124 was heavily rotted and drained rapidly when cored. Ambient air temperature during sampling was $-1.0 - -1.3^{\circ}\text{C}$.

125 The last cores sampled in 2015 were collected on 14 July from both ponded and non-ponded areas of a thin, clean floe (JY14-L4).
126 Ice collected in non-ponded areas ranged from 80–83 cm thick and was similar in character to the non-ponded ice of the other July
127 floes. Ice collected in ponded areas (under 5 cm water) ranged from 69–72 cm thick and was similar in character to the ice
128 collected from beneath melt ponds in the other July floes.

2.1.4 July 2017

129 In summer 2017, our team returned to the offshore waters near Utqiaġvik in search of ice that had previously broken from shore
130 and was continuing to melt (Fig. 3). A trip on 13 July 2017 yielded samples from five distinct ice floes of varying degrees of melt.
131 Ice thicknesses ranged from 40 cm to 110 cm. Seawater in open areas between floes had a salinity of 29.5 ppt and temperature of
132 $+4.8^{\circ}\text{C}$, as measured with a conductivity meter (YSI Model 30). Sampling on 17 July 2017 yielded ice from a single floe with
133 sample thickness varying between 62 and 110 cm. Pacific loons and bearded seals were observed in the vicinity.

2.2 Physical properties

2.2.1 Temperature, salinity, and density profiles

134 One core from each sampling site was used to measure vertical profiles of temperature, density, salinity, and pH. Ice temperature
135 was measured in the field immediately following core removal. The core was placed on a PVC cradle, and temperature was
136 measured using a field temperature probe (Traceable™ Total-Range Thermometer, Fisher Scientific; accuracy $\pm 1^{\circ}\text{C}$, resolution
137 0.1°C) inserted promptly into 3 mm diameter holes drilled into the center of the core at 5 cm intervals. Horizontal pucks of the ice
138 were then sawed at the 5 cm marks, and caliper measurements were taken of two thicknesses and two diameters across the puck to
139 estimate puck volume. Pucks were then sealed in Whirlpak bags and returned to the lab, where mass and salinity measurements
140 were taken of melted pucks using a digital scale and conductivity meter (YSI Model 30, accuracy $\pm 0.2\%$, resolution 0.1 ppt).
141 Bulk density was computed from the mass and volume measurements.

2.2.2 Thin section microphotography

142 Representative horizontal and vertical sections were prepared from each horizon of ice for each of the three time points sampled in
143 2015. Thin sections were prepared using a microtome (Leica), with the exception of some July samples that were too fragile for
144 microtome cutting. These fragile sections were cut as thin as possible on a chop saw (~ 1 cm thickness). All cut sections were then
145 photographed on a light table at working temperatures for each month as well as at -15°C . An LED epifluorescence microscope
146 (AxioScope.A1 LED, Carl Zeiss, with EC Plan-Neofluar phase contrast objectives) specially adapted for cold room work was



147 used to image the thin section samples. Transmitted light photomicrograph mosaic images were constructed from 50x
148 magnification snapshots taken at the working temperatures for each time point. Image software (ImageJ, Adobe Photoshop CC)
149 and manual image analysis were used to highlight pore spaces for pore size analysis.

2.2.3 X-ray micro-computed tomography

150 To prepare samples for x-ray micro-computed tomography (“micro-CT”) imaging, 10-cm subsections of ice cores returned from
151 the field were stored overnight in insulated coolers in a walk-in freezer set to working temperatures. Subsections were then placed
152 upright in Teflon centrifuge cups (500 mL bottles with tops cut off) and spun out at -5 °C for 5 minutes at 1500 rpm to remove
153 brine using a Thermoscientific S40R centrifuge. The masses of brine and spun-out ice were determined, and brines saved for later
154 analysis. Spun-out ice horizons were returned to the working-temperature walk-in freezer, where they were then placed upright on
155 top of corrugated cardboard circles placed inside the Teflon centrifuge cups. Working temperature dimethyl phthalate (DMP) was
156 then carefully poured down the sides of the container in order to flood the ice samples and form casts of the brine networks in
157 contact with the borders of the ice core as described by *Heggli et al.*, [2009] for casting snow. The DMP was left to penetrate
158 brine networks and slowly freeze at the working temperature for at least 12 hours before freezing fully at -20 °C. Casted cores
159 were then removed from the Teflon cups, sealed in Whirlpak bags, and stored at -20 °C for later imaging. In addition, several
160 archived cores from July 2015 that had been stored at -20 °C were scanned without casting to assess the effect of DMP casting on
161 tomography measurements.

162 Prepared samples were imaged at the U.S. Army Cold Regions Research Laboratory using a micro-computed tomography high-
163 energy x-ray scanner (SkyScan 1173, Bruker) housed in a -10°C walk-in freezer. Scans were run at 60 kV, 123 μA, with a 200 ms
164 exposure time and 0.6 ° rotation step. The nominal resolution was set to 142 μm pixel⁻¹ in a 560 x 560 pixel field of view, which
165 permitted fast scan times (18 minutes), resulting in low exposure of samples to excess radiation and egregious warming (scanner
166 chamber temperatures were recorded as ~2 °C during runs).

167 Shadow images generated by micro-CT were reconstructed into 2D horizontal slices using the software NRecon (Bruker).
168 Thermal abnormalities were corrected by performing x/y alignment with a reference scan. Samples with x/y shifts greater than
169 $|\Delta x| = 5$ were re-scanned. Following x/y alignment, reconstructed image histograms of linear attenuation coefficients were clipped
170 to 0.000 – 0.005 and the following correction factors were applied: 50 % defect pixel masking, 20 % beam-hardening correction,
171 smoothing level 2 using Gaussian kernel. Post-alignment shifts were determined manually and were between -2 and 2. The ring-
172 artifact reduction parameter was also chosen manually to minimize artifacts and was between 2 and 10 for all processed samples.

173 Reconstructed 8-bit 2D images were analyzed using the software CTAn (Bruker). Cylindrical subvolumes (height = 4.0 cm,
174 diameter = 4.97 cm) centered on the scanned sample’s z-axis were selected from the original scanned samples and positioned to
175 capture a representative segment of the sample, avoiding sample edges. Reconstructed images were parsed into four phases using
176 brightness thresholding determined manually at well-defined phase local minima for each scan: air (black), ice (dark grey), DMP



177 (bright grey), and brine (bright). Due to relatively large variability in brightness and contrast in reconstructed images as well as
178 poor brightness separation between the ice and DMP phases, manual thresholding was found to give more reliable results than
179 automated thresholding methods. Noise reduction was then applied using a despeckle of 8 voxels for ice, brine, and air, and 10^6
180 voxels for DMP (a high despeckle value ensured that only DMP-thresholded regions that connected to subvolume boundaries
181 were included, as any DMP “islands” are, by definition, artifacts). During the casting using DMP, air bubbles were trapped inside
182 the solidifying DMP. Due to the brightness order of phases (air > ice > DMP > brine) the gradient between air and DMP is
183 incorrectly identified as ice creating thin ice “rings” inside DMP regions of the 2D slices. This problem was resolved by using a
184 morphological operation called “closing”, where thin (1–2 pixel) threads of ice were dilated then eroded, thus removing the
185 features [Soille, 2003].

186 CTAn was then used to calculate properties of the parsed phases, including 3D volume, number of 3D objects, closed and open
187 porosity, and anisotropy. A description of the mathematical basis for these parameters as well as detailed best-practice methods
188 for micro-CT imaging of sea ice can be found in *Lieb-Lappen et al.* [2017].

189 Further, 3D prints of the reconstructed ice-only phase were made from the micro-CT reconstructions using polylactic acid fused
190 deposition modeling (Flashforge Creator Pro, FDM print with Makerbot print program and layer height 0.1 mm).

2.3 Optical properties

191 Field measurements of optical properties are typically limited to estimation of apparent optical properties (AOPs), e.g., albedo,
192 transmittance, and extinction. Due to the tenuous working conditions on rotten sea ice floes and instrument reliability problems,
193 we were not successful at obtaining estimates of *in situ* AOPs of rotten ice. As a result, our optical property measurement suite
194 focused on assessment of extracted cores in the laboratory. Inherent optical properties (IOPs), such as scattering and absorption
195 coefficients and scattering phase functions, are intrinsically difficult to measure in multiple-scattering media, but estimates from
196 laboratory measurements can build a picture of the evolution of sea ice independent of boundary conditions (e.g., ice thickness
197 and floe size) and the magnitude, directionality, and spectral character of the incident light field (see e.g., *Light et al.*, 2015).

198 The progression of light scattering properties of sea ice as it melts determines the partitioning of solar radiation in the ice-ocean
199 system. *Light et al.*, [2004] considered the evolution of the optical properties of sea ice samples as they warmed in a laboratory
200 setting, but encountered practical limitations for handling small samples of ice with large void space. The present study
201 specifically focused on techniques to extend the assessment of optical properties of sea ice in its advanced stages of melt.

202 To track the evolution of how the ice in this study partitioned sunlight, a laboratory optics study was carried out. Cores for optical
203 property assessment were sampled alongside cores for other characterizations, returned to the lab, and stored intact at -20 °C. The
204 May and June cores were stored for 2–3 days prior to running the optics experiments. The July cores were shipped back to the
205 freezer laboratory at the University of Washington and stored for 16 months prior to optical assessment.



206 To carry out optical property measurement, each core was cut into 10 cm thick sections. Each section was placed in a chamber for
207 the measurement of light transmittance using a technique developed to infer inherent scattering properties of a sea ice sample from
208 a simple measurement and a corresponding model calculation (see *Light et al.*, 2015). Spectral light transmittance between 400
209 and 1000 nm wavelength of each subsample was recorded relative to the transmittance through pure liquid water. The relative
210 transmittance was then compared with results from numerical radiative transport simulations using the model described by *Light*
211 *et al.*, [2004] for a wide range of scattering coefficients. The scattering coefficient producing relative transmittance (at 550 nm)
212 closest to the observed relative transmittance was then chosen. When subsamples from a full length of ice core are measured, this
213 technique estimates the vertical profile of the light scattering coefficient through the depth of the ice. By directly assessing
214 scattering coefficient, an IOP, we avoid complications introduced by the interpretation of AOPs (e.g., albedo, total transmittance
215 measured *in situ*), notably differences in total ice thickness and incident solar radiation conditions (e.g., diffuse/direct), as well as
216 other physical boundary conditions. In each case, samples taken from ice sitting below freeboard were placed into the sample
217 chamber and then gently flooded with a sodium chloride and water mixture in freezing equilibrium (temperature and salinity) with
218 the sample. Sample measurement was fast, with each sample in the chamber for less than one minute.

219 Samples were run in two modes. In the first mode, samples were analyzed promptly after removal from the ice. These samples
220 represent snapshots of the rotting process as it occurs naturally. The second mode was run in attempt to use light scattering
221 measurements to inform our understanding of ice rotting processes. To do this, an archived May core was cut into 10 cm thick
222 sections and placed in an insulated box in the freezer laboratory. The sections were stored standing upright and were placed on a
223 wire rack such that the melt water drained away from the remaining sample material. Initially, the freezer temperature was set to -
224 8 °C, but once the experiment commenced, the temperature was increased gradually every 24 hours. The sample density and
225 vertical scattering profile were measured at each temperature step (-6, -5, -4, -3, -2 °C over a one week period.) This attempt to
226 artificially rot the ice was documented using the optical measurements with the hope that such a measurement would inform our
227 efforts to simulate rotten ice in the laboratory.

3 Results

3.1 Ice core samples

228 Figure 4 shows photomosaics of representative cores collected at the different time points and from different rotten floes. The
229 series shows the progression from recognizable congelation ice in May, to the development of a retextured snow layer in June, to
230 the chaotic appearance of the ice structure in July.

3.1.1 May

231 In May, the interior of the ice was relatively translucent due to the small, isolated nature of brine and gas inclusions, a result of the
232 still relatively low temperature of the ice. Obvious brighter white bands of concentrated bubbles were present within the ice. A
233 weak layer was present in several cores between roughly 32–45 cm, which defined breaking points of the corresponding middle



234 horizon samples. May cores also exhibited a brown discoloration in the ice proximal to the ice-ocean interface which is indicative
235 of algae; this was confirmed by observation via microscopy of abundant pennate diatoms in ice bottom samples.

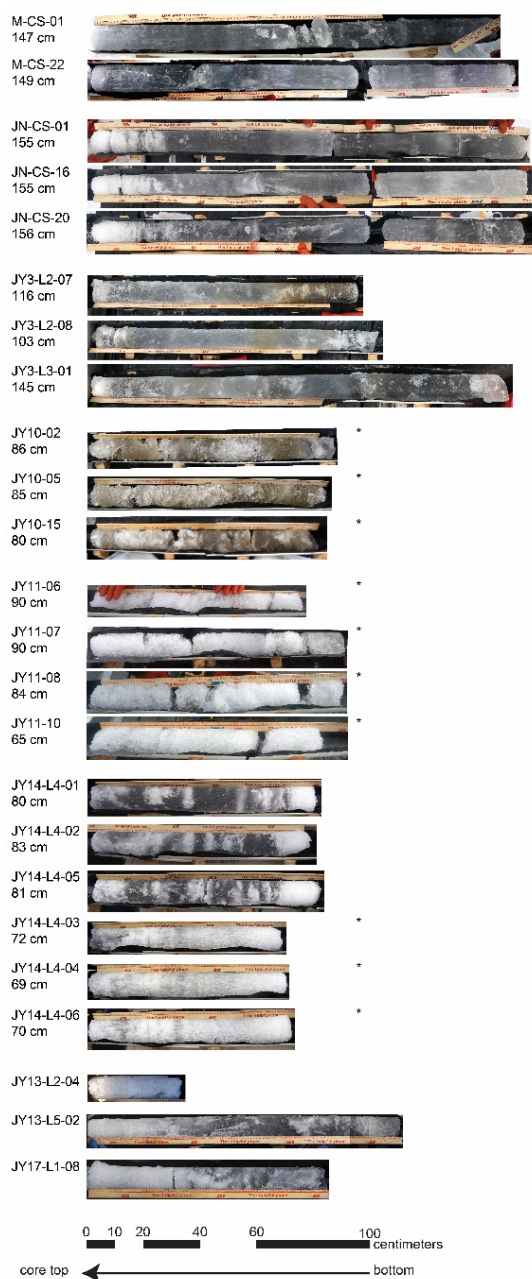
3.1.2 June

236 In June, the ice interior did not appear visibly distinct from May ice except for the upper surface of the ice. Significant rains
237 during the last week of May fell on the snow-covered ice, saturated the snow, and refroze. This produced a retextured snow layer
238 that occupied the upper 20 cm of the ice and was composed of grainy, bright ice with low structural integrity. Ice below the
239 retextured snow layer was soft and saline. Telltale discoloration in the bottom ~2 cm of sampled cores, albeit fainter than May,
240 indicates the algal cells had not yet completely sloughed from the ice. Additionally, green coloration of collected seawater
241 indicated the presence of an algal bloom in the melt water (7 ppt, 0.0 °C) at the base of the ice.

3.1.3 July

242 Ice collected in July 2015 and July 2017 was highly variable. Cores collected on 3 July 2015 were largely similar in character to
243 samples collected in June, including an apparent retextured snow layer in the upper ~10 cm of the ice. The ice-bottom algal
244 discoloration present in the May and June ice, however, was absent in July. Seawater was optically clear (no apparent algal
245 bloom), with a measured temperature of 1.5 – 4 °C between floes and 0.2 °C directly below several sampled floes.

246 Ice sampled in mid-July in both 2015 and 2017 was found to be in various stages of rot. Ice sampled from thick floes was similar
247 in character to the June 2015 and 3 July 2015 ice in non-ponded regions, but distinctly rotten below melt ponds. Uniformly thin
248 floes were rotten throughout in both ponded and non-ponded regions. Visually, rotten ice was devoid of the microstructural
249 inclusions that characterized the May and June ice interior, instead appearing to have large, isolated pores,



250

251 Figure 4. Photomosaics of representative cores collected and analyzed in this study showing the sequence of rot. Core names
 252 correspond to samples discussed elsewhere in this paper and are coded by sample site (as shown in Figure 1). The measured ice
 253 thickness at each core hole is indicated; due to variability in the ice bottom, spreading or loss of weak layers, and artefacts of
 254 image stitching, core images, which are shown to scale, may not match the measured ice thickness. Asterisks (*) indicate cores
 255 collected from submerged ice. Note the brown algal bloom layer visible in the bottom of the May core and faintly visible at the
 256 bottom of the June core, and the bright layer of retextured snow at the top of the June cores.

257



258 and a more chaotic structure. When cored, rotten ice crumbled or broke at many points along the length of cores, rendering it
259 difficult to handle. Rotten ice drained copiously when cores were removed from drill holes, and the bottom portion of rotten cores
260 consisted of optically clear, fresh ice drained of brine and characterized by large (cm-scale) voids. Figure 5 shows photomosaics
261 of cores sampled on 14 July 2015 at Location 3. Images show variations in ice texture depending on whether the ice was ponded
262 or non-ponded, although both types do appear to have at least some scattering layer with bright white appearance.

3.2 Physical properties

3.2.1 Temperature, salinity, and density profiles

263 The May temperature profile had values as low as $-8\text{ }^{\circ}\text{C}$ at the snow-ice interface; below that, temperatures increased with depth
264 (Fig. 6). By June, the entire depth of the ice had warmed above $-1\text{ }^{\circ}\text{C}$, with the lowest temperatures measured in the middle
265 sections of cores. By July, the ice was approximately isothermal, with temperature $0\text{ }^{\circ}\text{C}$. These profiles generally agree with
266 observations at the MBS and are typical of other investigations in the area (e.g., *Zhou et al.*, 2013).

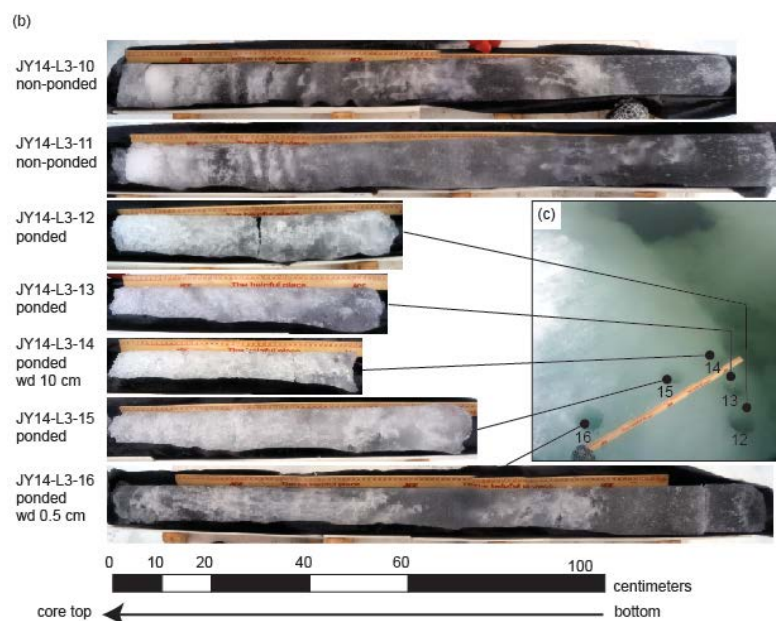
267 Bulk salinity profiles (Fig. 6b) were also consistent with prior published observations. May ice showed the classical C-shaped
268 salinity profile with enhanced salt content near the upper and lower boundaries (10 ppt) and lower salt content ($< 5\text{ ppt}$) in the
269 interior of the ice. By June, significant fresh water flushing from rain and snow melt reduced the salt content in the upper portions
270 of the ice. The July profiles showed evidence of prolonged flushing, with salt content approaching zero in some cores.

271 Density values (Fig. 6c) measured in this study in May and June averaged 0.91 and 0.87 g cm^{-3} , respectively, with the lowest
272 density values (as low as 0.63 g cm^{-3}) found in the uppermost portions of the June core. Relative measurement errors calculated
273 for May and June samples were typically $< 6\%$ in May and $< 10\%$ in June except for a few outliers, while July samples had many
274 samples with measurement errors $> 10\%$ because of difficulty determining a volume for the irregular sample shapes.

3.2.2 Thin section microphotography

275 Thin sections show the evolution of the ice structure as it warmed (Fig. 7). Each of the microphotographs in Fig. 7 is a stitched
276 composite of 20 individual images taken at 25x magnification. The May and June images clearly show individual brine and gas
277 inclusions.

278 Inclusions in the May sample had average size of $80\text{ }\mu\text{m}$ ($9\text{--}577\text{ }\mu\text{m}$, standard deviation $62\text{ }\mu\text{m}$, 162 inclusions resolved) with an
279 inclusion number density of 32 mm^{-3} . The average size of inclusions in the June sample increased to $221\text{ }\mu\text{m}$ ($61\text{--}587\text{ }\mu\text{m}$,
280 standard deviation $105\text{ }\mu\text{m}$, 103 inclusions resolved) while the number density decreased to 19 mm^{-3} . The July sample exhibited
281 notably larger and fewer inclusions. Because they were so large, however, it was difficult to characterize a

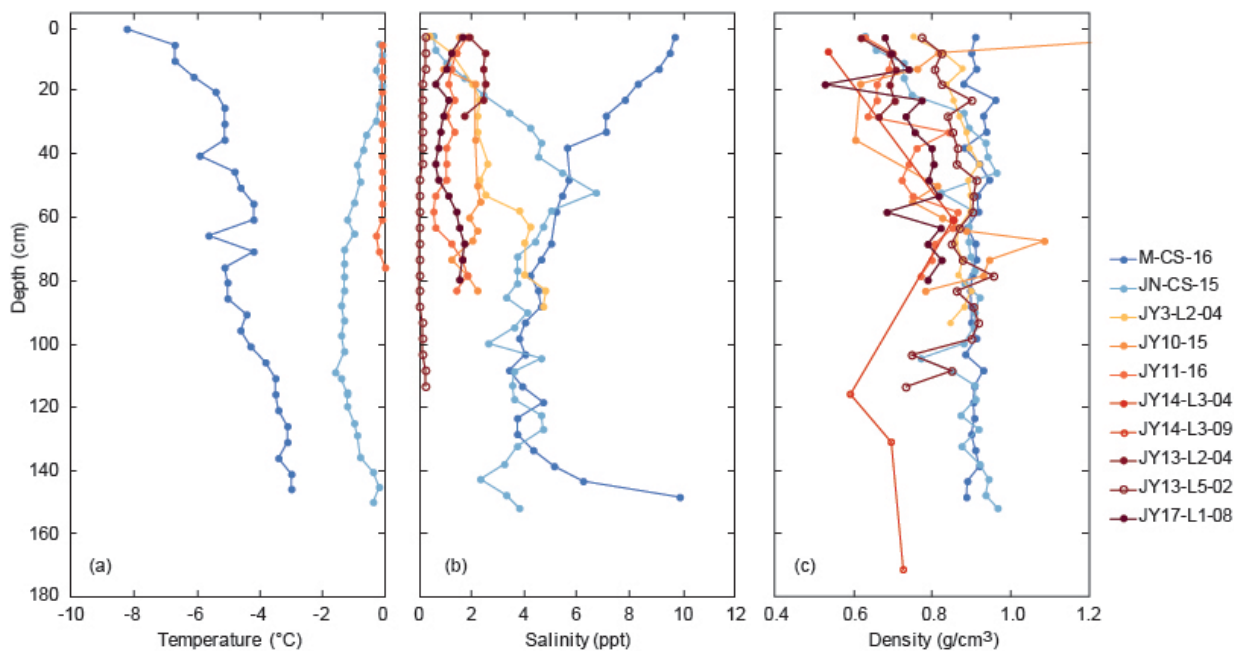


282

283 Figure 5. (a) Photograph of the part of a rotten floe sampled on 14 July 2015 (JY14-L3). Poned and non-ponded areas visible in
284 the picture were drilled for core samples. (b) Several cores drilled from JY14-L3 floe (JY14-L3-10–JY14-L3-16) showing the
285 variability in length and character of ice from non-ponded areas vs. from beneath pelt ponds. (c) Region of poned ice that was
286 drilled to collect the poned ice cores shown in (b). Cores JY14-L3-12–JY14-L3-14 were drilled from ice at a water depth (“wd”
287 in legend) of ~10 cm, JY14-L3-15 was drilled from intermediate depth, and JY14-L3-16 was drilled from a water depth of ~0.5
288 cm.

289

290



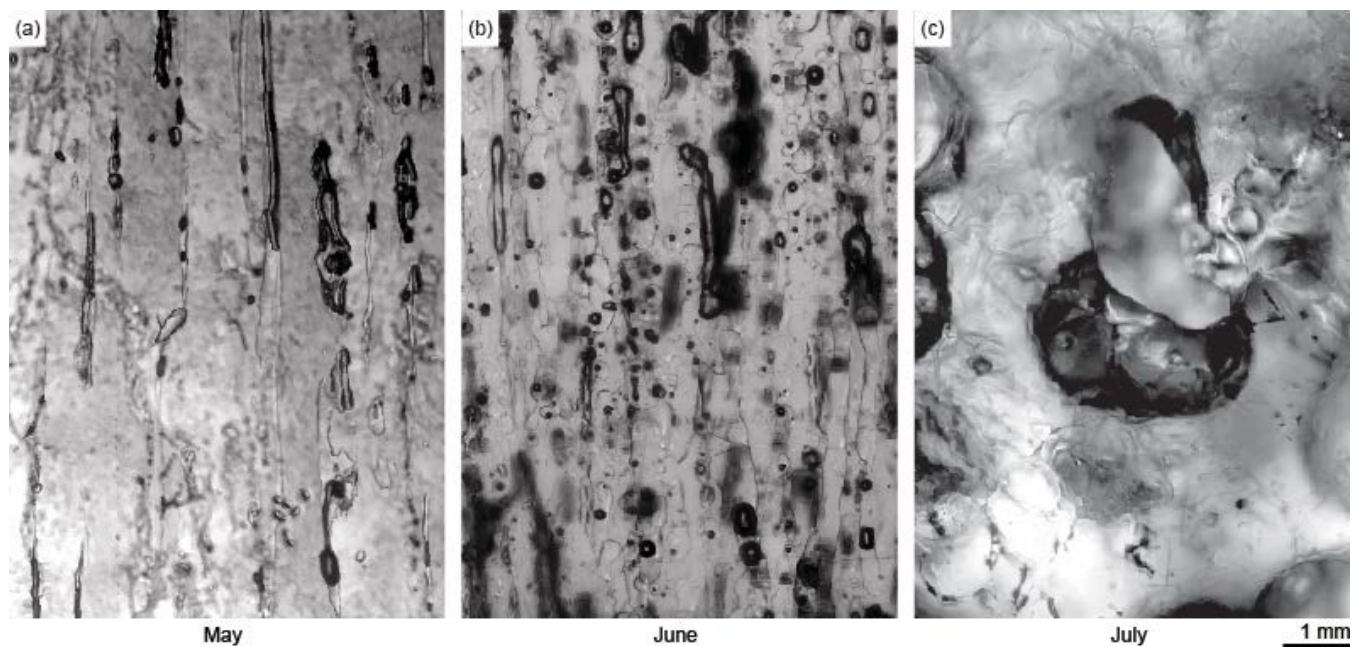
291

292 Figure 6. Ice core profiles of (a) temperature, (b) salinity, and (c) density showing changes in ice properties over the course of
293 summer melt from May (M-CS-16, dark blue), June (JN-CS-15, light blue), July 2015 (3 July core, JY3-L2-04, yellow; 10 July
294 rotten core from sediment-rich, ponded ice, JY10-15, orange; 11 July rotten core from ponded ice, JY11-16, red; 14 July rotten
295 core from ponded ice, JY14-L3-04, dark red, filled circle; 14 July rotten core from non-ponded ice, JY14-L3-09, dark red, open
296 circle), and July 2017 (13 July Floe 2 JY13-L2-04, magenta, filled circle; 13 July Floe 5 JY13-L5-02, magenta, open circle; 17
297 July Floe JY17-L1-08, purple).
298

299 significant number of inclusions in any given sample. In the sample that was analyzed, only nine individual inclusions were
300 completely resolved. Despite poor statistics, the average size of the inclusions in the July sample was 3 mm (range 1–5 mm) and
301 the estimated inclusion number density was 0.01 mm⁻³. The reduced number of resolved inclusions with time is expected as the
302 inclusions enlarge (due to freezing equilibrium) and merge. Additionally, the July section was necessarily thick, such that imaging
303 in transmitted light was challenging.

3.2.3 X-ray micro-computed tomography

304 Calculations done on 3D reconstructions generated from micro-CT show a significant evolution in the internal structure of ice
305 during the course of melt and help define “rotten” ice. Figure 8 shows reconstructions of the ice-only phase (top row),
306 reconstruction of the not-ice phase (air + brine + DMP) with objects of different sizes color coded as blue (<0.11 cm³), green
307 (0.11–1.15 cm³), and red (>1.15 cm³) showing the evolution toward larger pores and channels in rotting ice (middle row).



308

309 Figure 7. Ice sample vertical thin section transmitted light photomicrograph mosaics from May, June, and July ice samples, shown
310 at the same scale. (a) Vertical thin section from middle horizon of M-CS-8 core (depth = 32–52 cm) showing vertical brine
311 channels. (b) Vertical thin section from middle horizon of JN-CS-22 core (depth = 45–65 cm) showing enlarged brine channels.
312 (c) Vertical thin section from middle horizon of JY10-CS-11 (depth = 32–42 cm) showing pore space.

313

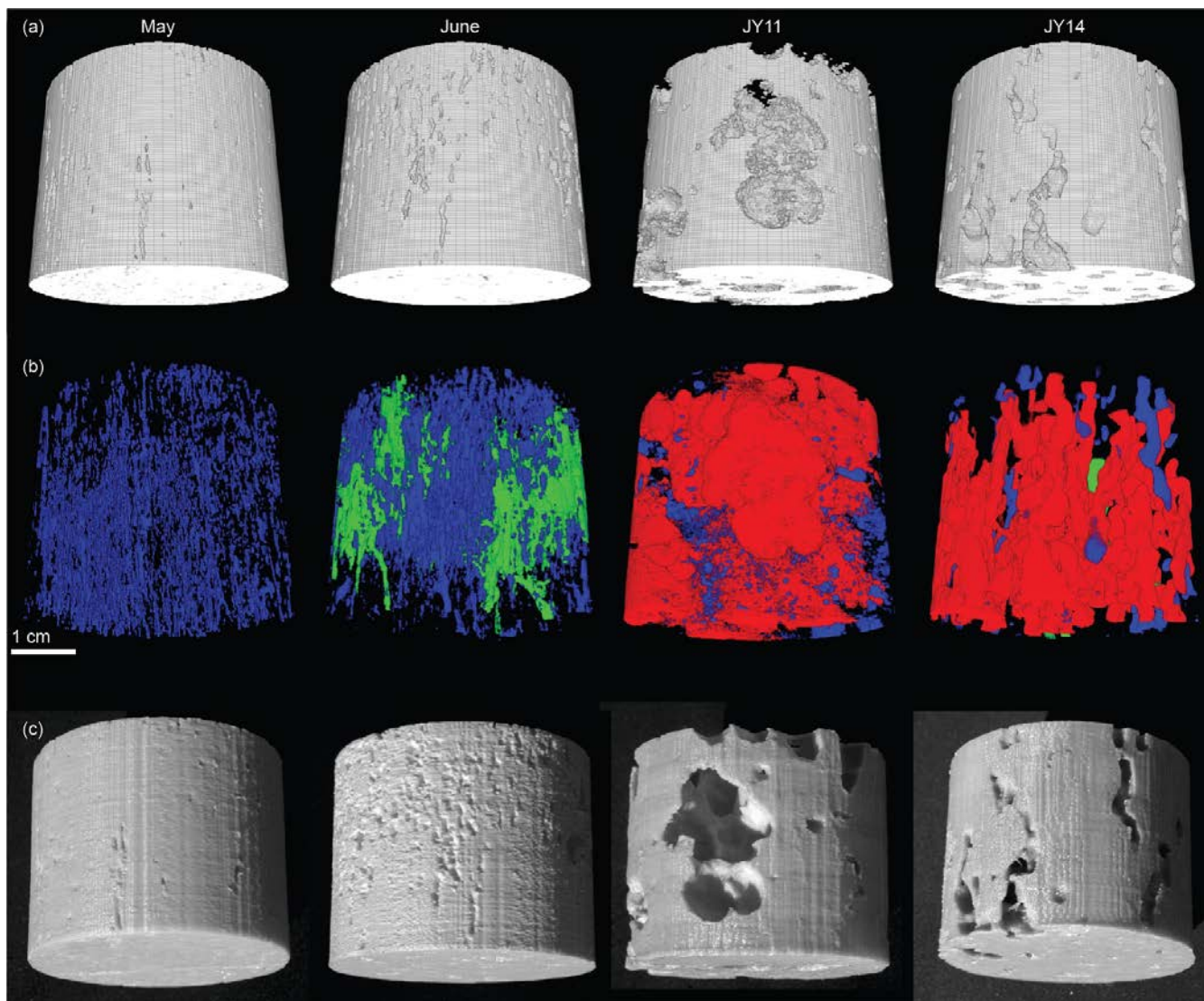
314 Note that micro-CT analyses only resolve structures with a short dimension $> 284 \mu\text{m}$, (derived from the 8 voxel despeckle that
315 was applied) which is significantly larger than the average inclusion size observed in the microscope imagery for both May and
316 June. The bottom row shows monochrome photographs of 3D prints made from the four reconstructions.

317 Porosity is defined as the percentage of total volume occupied by pores, as measured from the ice-only phase perspective such that
318 the porous space is derived from air, brine, and DMP. Porosity in DMP-casted May and June horizons (excluding June top
319 horizons determined to represent a retextured snow layer) ranged from 0.5–7.5 % by volume (Fig. 9a). In contrast, the DMP-
320 casted rotten core (JY11-06) had a range in porosity of 37.5–47.9 %. For non-casted rotten cores measured, the porosity ranged
321 from 7.6–23.1% (mean = 15.5 %) in a sample collected from below a melt pond (JY11-19), and from 5.7–46.0 % (mean = 21.6
322 %) in samples collected from bare, non-ponded ice (JY13-2 and JY13-4). Bare ice had the highest porosity values in the upper 10
323 cm (24.7–46.0 %), corresponding with a retextured snow layer. Similarly, two sample volumes selected from retextured snow
324 layers of June ice exhibited extremely high porosity values of 48.9 % and 53.6 %.

325 In addition to becoming generally more porous, the nature of pores in the ice changes as the melt progresses. The ratio by volume
326 (V/V) of open pores (indicating connection to the surrounding ice volume) to closed pores (pores contained wholly



327

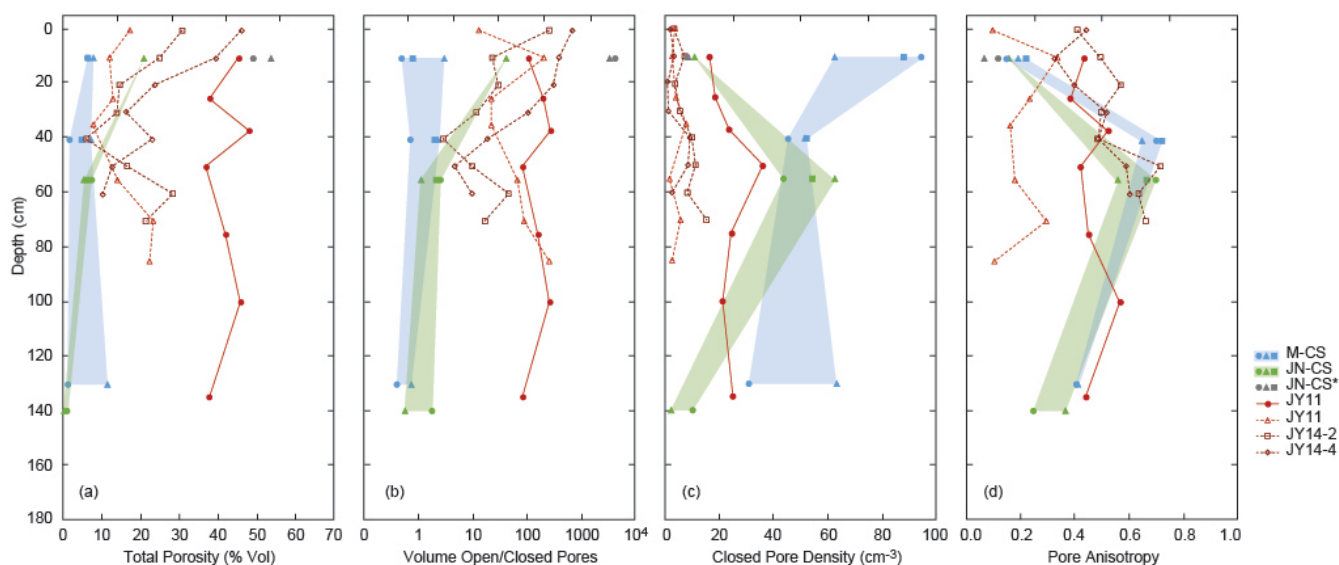


328

329 Figure 8. 3D reconstructions from micro-CT scans of middle horizon cuts of cores collected in May, June, and July (JY11 and
330 JY14) 2015 showing the evolution of pore space. Series (a) shows the reconstruction of the ice-only phase. Series (b) shows the
331 reconstruction of the not-ice phase (air + brine + DMP) with objects of different sizes color coded as blue ($<0.11 \text{ cm}^3$), green
332 ($0.11\text{--}1.15 \text{ cm}^3$), and red ($>1.15 \text{ cm}^3$) showing the evolution toward larger pores and channels in rotten ice. Series (c) shows
333 monochrome photographs of 3D prints of the reconstructed ice-only phase.

334

335



336

337 Figure 9. Sea ice internal pore properties calculated from 3D reconstructions of micro-CT scans of cuts of cores collected in May,
 338 June, and July. (a) Total porosity as percent of the analyzed volume. (b) Volume of open pores vs. closed pores in the analyzed
 339 volume. (c) Average spatial density of closed pores in the analyzed volume. (d) Anisotropy of pores in the analyzed volume.
 340 Depths indicate the in situ depth within the ice of the top of the volume of interest for which the calculations were done. Colors
 341 indicate sampling month: May (M-CS; blue), June (JN-CS; green), and July (JY11 and JY14; red and dark red, respectively).
 342 Shaded blue and green fields represent the range of values measured in replicate ice horizon samples in May and June,
 343 respectively. Closed markers indicate DMP-casted samples; open markers indicate un-casted samples. Values calculated from a
 344 volume believed to be representative of a retextured snow layer in the uppermost June samples are represented by grey
 345 symbols. For all points, the volume analyzed was a 77.6 cm³ cylinder (diameter = 4.97 cm, height = 4.0 cm) selected from a
 346 representative portion of the interior of the cut sea ice horizon.

347

348 within the 77.6 cm³ volumes analyzed) is similar in May and June (Fig. 9b; 0.9–2.9 in May with mean = 1.2, 0.5–2.3 in June
 349 middle and bottom horizons with mean = 1.3) with the exception of the June upper horizon retextured snow layer. In July’s rotten
 350 ice, however, the volume ratio of open to closed pores increased dramatically (2.7–276.8, mean = 105.3). In addition, the number
 351 of closed pores in the normalized unit volume decreases from May and June to July (Fig. 9c). The May cores and June middle
 352 horizons have the highest closed pore densities (31–94 cm⁻³ with mean = 61 cm⁻³, and 2–63 cm⁻³ with mean = 26 cm⁻³ in May
 353 cores and 44–63 cm⁻³ measured in June middle horizons). In June, the density of closed pores in the top and bottom (8–11 cm⁻³,
 354 and 2–10 cm⁻³, respectively) decrease, creating a reverse C-shaped profile. In July, the density of closed pores is uniformly low
 355 throughout the cores measured (16–36 cm⁻³ with mean = 24 cm⁻³, and 1–16 cm⁻³ with mean = 6 cm⁻³ in casted and non-casted July
 356 cores, respectively). Both metrics indicate that connected (open) pores dominate in July. This follows from larger pore sizes, as
 357 quantified by the 2D structure thickness metric, which measures the mean maximum diameter of 3D objects. In May and June,
 358 pores averaged <5 mm along their longest axis (1.7–3.3 mm, mean = 2.4 mm, again with the exception of the June retextured



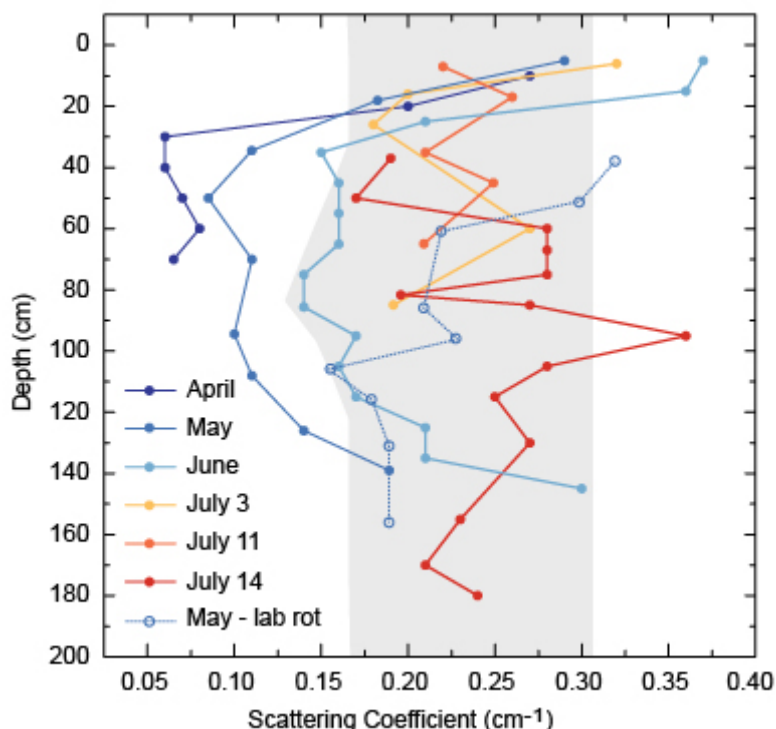
359 surface snow and a 32 mm outlier value in one June middle horizon). In rotten July cores, pores enlarge substantially (4.2–17.0
360 mm, mean = 8.1 mm). The trend toward more connected pores is most pronounced in the upper- and lowermost layers of the core.

361 Anisotropy roughly indicates deviation from spherical structures, with a value of 0 indicating a perfectly isotropic sample
362 (identical in all directions) and 1 indicating a perfectly anisotropic sample (fully columnar). In sea ice, the highest degree of
363 anisotropy corresponds to elongated brine channels in columnar ice [Lieb-Lappen *et al.*, 2017]. Anisotropy (Fig. 9d) in the not-ice
364 fraction (air + brine + DMP) of May and June samples followed a reverse C-shaped profile (cf. Lieb-Lappen *et al.*, 2017), with the
365 highest degree of anisotropy found in middle horizons (0.43–0.72) and lower anisotropy in the top and bottom horizons
366 (0.14–0.41). In the rotten July cores, the C-shaped profile disappeared. In the JY11 sample analyzed (from ponded ice), the
367 middle portion of the core became more isotropic (0.38–0.57 in the DMP-casted sample, 0.24–0.34 in the uncasted sample),
368 indicating a rounding of the core center brine channels. This trend was not apparent in the JY14 (thinner rotten floe of non-ponded
369 ice) sample, however, in all July cores analyzed, the upper layer had a generally greater anisotropy value than core middle values,
370 perhaps indicative of vertical channel formation in the upper portion of the ice due to melt and draining from the upper portion of
371 the ice.

3.3 Optical properties

372 As the sea ice cover progresses through the onset and duration of melt season, its optical properties respond to increased
373 temperature and the absorption of increasing amounts of solar radiation. Typically, the albedo of the ice cover decreases (less light
374 backscattered to the atmosphere) and its transmittance increases (more light propagating into the ocean). The bulk of this effect,
375 however, is due to the loss of accumulated snow and the widespread formation of melt puddles on the ice surface [Perovich *et al.*,
376 2002]. While this net effect dominates the surface radiation balance, it overlooks effects due to changes in the properties of the ice
377 itself. As the ice warms and becomes porous, permeable, and rotten, increases in void space increase the total amount of internal
378 ice / liquid boundary, and would thus be expected to increase total scattering. Increases in ice scattering should promote higher
379 albedo and lower transmittance—exactly opposite the behavior of the aggregate ice cover.

380 The results of the laboratory optical measurements are shown in Fig. 10. Vertically resolved profiles of scattering coefficient are
381 shown for ice obtained in April, May, June, and July. The April ice was extracted in the same vicinity as the May and June
382 samples during unrelated field work in 2012. In addition to the temporal trend of sampled ice, optical property assessment was
383 also carried out for a May sample that was later subjected to controlled melt in the laboratory (open circles). Scattering
384 coefficients generally increased with time and individual profiles were typified by the characteristic c-shape (higher scattering at
385 top and bottom of the column, lower scattering in the middle) also seen in typical salinity profiles.



386

Figure 10. Vertically resolved scattering coefficients of sea ice measured during each phase of the field campaign. Coefficients are inferred from laboratory optical transmittance measurements (after Light et al., 2015) and interpretation of a radiative transport model in cylindrical domain (Light et al., 2003). April profile included to show spring ice was measured on ice sampled in 2012 at a comparable geographic location. The May lab rot profile is for ice extracted in May during field campaign, and then warmed in the lab prior to sub-sample preparation. Shaded area shows the range of measurements on melting multiyear ice (Light et al., 2008) and melting first-year ice (Light et al., 2015).

387

4 Discussion

4.1 Physical characteristics of rotten ice

388 As sea ice warms, its microstructure changes as inclusions of brine and gas enlarge as required to maintain freezing equilibrium.
389 This has been well established theoretically [Cox and Weeks, 1983], as well as in laboratory experiments [Perovich and Gow,
390 1996; Light et al., 2003] for ice with isolated inclusions of brine and gas. This study addresses the limits of sea ice microstructure
391 when natural ice is in advanced stages of melt, where these inclusions are typically no longer isolated, but rather are in connection
392 with the ocean and/or the atmosphere.

393 The equations of Cox and Weeks [1983] describe the phase relations of sea ice for temperatures less than or equal to $-2\text{ }^{\circ}\text{C}$ and
394 where the bulk ice density describes a volume containing liquid brine and gas—both in equilibrium (freezing equilibrium with the
395 ice in the case of brine and phase equilibrium with the brine in the case of gas). In the case of ice in advanced melt, the ice



396 temperature would be expected to be always close to 0 °C. Furthermore, most sample volumes will typically include void spaces
397 that are in connection with the atmosphere or ocean and hence may not conform to the requirements of freezing or phase
398 equilibrium (e.g., brine inclusion size will not necessarily shrink if the temperature decreases). As a result, expected changes in the
399 microstructure—and ultimately, the mechanical behavior—of sea ice at most times of the year are not expected to pertain to changes
400 experienced during late summer.

401 Photos of ice core samples shown in Fig. 4 illustrate the evolution of the ice structure. Early in the season, the majority of the
402 interior ice (areas away from the top and bottom) appears mostly translucent and often milky with the exception of isolated bright,
403 bubble-rich weak layers. As the season progresses, more of the ice appears opaque, losing its transparency (Fig. 4). This highly
404 scattering ice results from merging, connecting, and draining inclusions. This effect is clearly seen in the cores that were
405 submerged when extracted (e.g., the cores indicated with * in Fig. 4, and cores shown in Fig. 5), but can also be seen in the JY13-
406 L1 and JY13-L2 cores, which were not submerged when sampled.

407 Submerged cores appear to have more porous ice structure. We hypothesize this is due to additional heating of submerged ice.
408 This heating may come as a result of increased absorption of radiation as swamped or ponded ice will not maintain a substantial
409 surface scattering layer, and as a result, its albedo is typically lower [*Light et al.*, 2015], and more sunlight is absorbed within its
410 interior. Or it may result simply from the contact between this ice and sunlight-warmed water. It is also possible this additional
411 melting serves to enhance the connectivity of this ice to the ocean, promoting the invasion of seawater—and any associated
412 heat—from beneath.

4.1.1 Temperature, salinity, and density profiles

413 Rotten ice is isothermal, having warmed to approximately the freezing temperature (0 °C) of fresh water. Correspondingly, core
414 samples of rotten ice extracted from the ocean typically drain any associated liquid rapidly. Accordingly, this ice is much fresher
415 than earlier-season ice, with salinity values < 3 ppt through most of the core, indicative of a loss of much of the brine that
416 characterizes earlier-season ice (see Fig. 6b). The May salinity measurements show the classic ‘c-shaped’ salinity profile
417 indicative of first-year ice yet to experience summer melt. By June, the salinity profile shows freshening at the ice bottom, likely
418 associated with the onset of bottom ablation. Additionally, the top of the June ice shows significant freshening. In this particular
419 year at this location, this change is likely related to the presence of retextured snow at the ice surface, which would be expected to
420 be very fresh. It may also result, in part, from the onset of surface ablation and the ensuing fresh water flushing that would be
421 expected this time of year. The July ice was almost completely devoid of salt. This is expected, due to the prevalence of a
422 connected pore structure and the significant flushing and drainage of virtually all salt in the ice.

423 Density profiles (Fig. 6c) reflect changes in temperature, bulk salinity, and structure. We observed a marked decrease in density
424 corresponding to summer melt, a result of the dramatic increase in porosity that defines rotten ice. May and June profiles had
425 density measurements centered around 0.9 g cm⁻³ and showed little variability except for reduced density in the upper portions of



426 the June core, likely resulting from the prevalence of the observed retextured snow. July profiles had even further reduced density,
427 with values reaching as low as 0.6 g cm^{-3} , reflecting void spaces in the ice following the rapid draining of seawater from the ice,
428 and was much more variable. For comparison, the density of core horizons (measured using the same technique) taken in melting
429 Arctic pack ice in July 2011 had similar values between $0.625\text{--}0.909 \text{ g cm}^{-3}$ [Light *et al.*, 2015]. Normally, sea ice with
430 significantly smaller bulk density would be expected to float higher in the water and thus have larger freeboard. But the density
431 reductions that occur during advanced melt result from large void spaces within the ice that are typically in connection with the
432 ocean. As a result, such ice can have small freeboard, even if total ice thickness is still relatively large.

433 It is worth noting that sediment loading did not appear to influence the density and structure of rotten ice. Rotten cores collected
434 on 10 July 2015 came from a floe with a visibly high sediment load, while rotten cores collected on 11 July 2015 and in July 2017
435 had much less sediment (Fig. 4). For all July cores, measured density values were similar within the large range of measurement
436 error. Salinity in the core collected from a sediment-rich floe was, however, somewhat higher than the cores collected from
437 “clean” floes.

4.1.2 Internal structure: porosity, connectivity and implications of rot

438 The number and size of brine inclusions identified in this study through the microscope imagery is commensurate with the number
439 and size of inclusions documented by Light *et al.* [2003]. That study reported a brine inclusion number density range of 24 mm^{-3}
440 to 50 mm^{-3} from ice sampled in May, offshore from Utqiagvik in a similar vicinity as the present study. The number densities
441 observed in May ice in the present study were 32 mm^{-3} in May, well within the range identified by the earlier study. The earlier
442 study showed brine inclusion number densities to decrease with increasing temperature, up to a point, but did not follow the ice
443 into advanced melt. The present study documents decreases in inclusion number density from 32 mm^{-3} in May to 19 mm^{-3} in June
444 to 0.01 mm^{-3} in July. While these values are consistent with the earlier findings, they also extend the results much further into melt
445 than has been previously attempted. In particular, the micro-CT work is useful for sampling much larger sample volumes, and thus
446 central for estimating size and number distributions for the July ice.

447 Porosity (Fig. 9a) is low in May, with values less than 10 %, and increases as the ice warms and melts. By July, the micro-CT-
448 determined porosity approached 50 %, commensurate with densities measured as low as 0.6 g cm^{-3} . There were differences in the
449 handling of cores used for direct density measurement and cores used for micro-CT imaging. In particular, cores used for density
450 measurement were extracted from the ice immediately prior to measuring their dimensions. In contrast, samples taken for micro-
451 CT imaging spent several hours transiting to the laboratory and core horizons to be casted were then centrifuged prior to casting
452 and subsequent imaging. Significant melting and drainage would likely have caused those cores to lose more liquid, but to also
453 have suffered some melt during transport to the laboratory. It would thus be expected that the micro-CT-derived porosity
454 measurements could yield estimates with less included fluid than the density measurements made closer to in situ conditions.
455 Similarly executed micro-CT measurements have quantified included air volumes in growing winter sea ice [Crabeck *et al.*,



456 2016], where the gas phase was clearly distinguished from the brine phase, but the total pore space did not increase above 11 %,
457 which is far smaller than the ultimate pore space observed in this study.

458 The permeability, and hence pore structure, is central to the hydrological evolution of summer sea ice [Eicken *et al.*, 2002]. This
459 suggests that the documentation of highly permeable ice with large porosity may be central to understanding the mass balance of
460 modern ice covers late in the summer melt season. In particular, Eicken *et al.* [2002] outlined a mechanism for significant ice melt
461 whereby warmed surface waters run off the ice and accumulate beneath areas with shallow draft late in summer, and this pool of
462 warmed fresh water experiences convective overturn and is entrained within the open structure of melting ice. It is expected that
463 further melting from this additional heat could exacerbate the decay and structural frailty of the melting ice, literally melting it
464 from the inside out.

465 The pore anisotropy results shown in Fig. 9d reinforce the overall trend that as the season progresses, the ice structure
466 homogenizes, losing its characteristic c-shape. Where strong vertical gradients in anisotropy existed in May and June, the July ice
467 is more uniform. Our findings are consistent with those of Jones *et al.* [2012], which used cross-borehole DC resistivity
468 tomography to observe increasing anisotropy of brine structure during spring warming. In that work, the brine phase was found to
469 be connected both vertically and horizontally and the dimensions of vertically oriented brine channels gradually increased as the
470 ice warmed.

471 There remain notable limitations associated with the characterization of sea ice using micro-CT techniques. Many small brine
472 inclusions were not counted owing to the limited spatial resolution of the technique. Furthermore, the casting technique that was
473 employed appears to have introduced artifacts, especially in connectivity. From all the derived properties (porosity, connectivity,
474 and anisotropy), it appears that the introduction of the casting media may have forced channels to enlarge and channel connections
475 to be established, where perhaps they did not exist naturally. However, the trend in casted samples and the values measured for
476 uncasted samples reflect the substantial changes in ice character that are apparent in the field.

4.2 Optical evolution of rotting ice

477 Increases in effective light scattering coefficient over the course of seasonal warming are shown to be approximately 5-fold for the
478 interior ice studied here (Fig. 10). The overall trend of increasing scattering with time as the melt progresses is a result of the
479 connecting and draining microstructure, as assessed in the microstructure and tomography analyses. Relative increases in the
480 scattering would be expected to scale by the inclusion number density multiplied by the effective inclusion radius squared (see
481 Light *et al.*, 2003). Using the observed mean inclusion sizes and number densities, we thus predict scattering increases with
482 factors of 4 and 6 for June and July, relative to May. The variability in both the inclusion distributions and the measured scattering
483 make this a difficult comparison, but the increased scattering shown in Fig. 10 is consistent with these predicted relative increases.

484 Early in the season, the larger scattering near the ice bottom likely reflects the higher brine content (larger and/or more numerous
485 brine inclusions) near the growth interface. The larger scattering near the top ice surface likely results from the less organized ice



486 structure that forms prior to the onset of congelation growth during initial ice formation. As the melt season progresses, this
487 uppermost portion of the ice has additional enhanced scattering due to the drainage of above-freeboard ice and the eventual
488 development of a surface scattering layer. The enhanced scattering at the top and bottom of the ice results in a C-shaped profile,
489 consistent with observed salinity profiles. This C-shape appears to dominate the profiles for April, May and June, but the July
490 sample appears to have no memory of the characteristic C-shape found earlier in the season. Given the significant structural
491 retexturing that occurred by July, this should not be surprising.

492 Laboratory optical measurements made analogously to the ones in this study were carried out for melting first-year sea ice in the
493 open pack (see [Light *et al.*, 2015]). That data set included little information about the temporal progression of the ice, as no one
494 location was sampled more than once. However, interior ice scattering coefficients between $0.1\text{--}0.3\text{ cm}^{-1}$ were found for that ice
495 in June and July, and these values are comparable to what was found in this study.

496 In an effort to use light scattering measurements to inform our understanding of ice rotting processes, we monitored the optical
497 properties of natural ice samples as they melted. Since most of the May core had *in situ* temperature $> -5\text{ }^{\circ}\text{C}$, only small changes
498 in sample density and light scattering properties were observed until the ice warmed to $-2\text{ }^{\circ}\text{C}$ (Fig. 10, dashed curve). The lab-rot
499 core shows significantly enhanced scattering, although not as large as the naturally rotted ice. This was viewed as a preliminary
500 attempt to create rotten ice in the laboratory.

5. Conclusions

501 As Arctic sea ice melts during the summer season, its microstructure, porosity, bulk density, salinity, and permeability undergo
502 significant evolution. *In situ* measurements of sea ice documented off the northern coast of Alaska in May, June, and July, indicate
503 that sea ice transitioned from having 4–10 ppt salinity in May to near zero salt content in July. The ice became extremely porous,
504 with porosity values exceeding 10 % through most of the depth of the ice compared to $<10\%$ for ice collected in May and June.
505 Some July porosity values approached 50 % at places in the ice interior. Brine pockets in rotten ice are few; the ice is essentially
506 fresh in composition and characterized by large, visible voids and channels on the order of several millimeters in diameter. These
507 changes result from increased air temperature, ocean heat, and prolonged exposure to sunlight and leave the ice with dramatically
508 increased porosity, pore space with increased connectivity, and increased capacity to backscatter light. These changes have
509 potential implications for the structural integrity, permeability to surface melt water as well as ocean water, light partitioning,
510 habitability, and melting behavior of late summer ice. Specifically, increased connectivity with the ocean may affect how material
511 (e.g., dissolved and particulate material, including biological organisms and their byproducts) is exchanged at the ice/ocean
512 boundary. Subsequent surface meltwater flushing may in turn effectively rinse these constituents from the ice, making this
513 enhanced connectivity central to the control of ice-associated constituents well into the summer season. Rotten ice is a very
514 different physical and chemical habitat for microbial communities than earlier-season ice.



515 Reductions in bulk density were observed to occur from values approximately $0.90\text{--}0.94\text{ g cm}^{-3}$ to values as low as 0.6 g cm^{-3} .
516 Pore spaces within this low density ice, however, were typically well connected to the ocean. This left the low-density summer ice
517 to generally have very small freeboard and frequently be flooded by ambient seawater. Finally, and significantly, field
518 observations stress the lack of structural integrity of this porous, fragile ice, indicating that thickness-based models of ice behavior
519 may not accurately predict the behavior of late-season sea ice.

520 In addition to sampling naturally rotted sea ice, we have also attempted to simulate the rotting process in the laboratory. Our
521 laboratory optics measurements suggest that natural samples extracted early in the season can be at least partially rotted in the
522 laboratory. To achieve ice that is as rotted and structurally compromised as was observed to occur in nature, the absorption of
523 solar radiation may be a necessary parameter. Sunlight is key to the formation of surface scattering layers at the air–ice interface.
524 In the lab, ice was permitted to rot in air, so any melt that was produced would quickly drain away. In nature, the ice necessarily
525 floats in its own melt, and this may be a critical difference. Increases in melt season length may bring increased occurrence of
526 rotten ice, and the timing and character of the seasonal demise of sea ice may be related to the evolution of the ice microstructure.

Data availability

527 Data archived at NSF Arctic Data Center <https://arcticdata.io/catalog/#view/doi:10.18739/A28C9R366>



Appendix

528 Table A1: Summary of sea ice sampling.

Sampling Date	Sampling Location	Ice Type
6 May 2015 Snowmachine	71°22.535' N 156°31.686' W	Landfast
11 June 2015 ATV	71°22.549' N 156°31.676' W	Landfast
3 July 2015 Vessel 'Kimmialuk'	71°22.549' N 156°31.676' W	~15 m ² white floe, 170 cm thick
	71°23.130' N 157°04.764' W (drift ~2.5 km/hr NE)	~2 m ² light brown floe, 86-150 cm thick
	71°18.033' N 155°38.081' W	145 cm thick ice
10 July 2015 Vessel 'Jenny Lee'	71°27.154' N 156°32.137' W (drift ~1 km/hr NNW)	Dirty floe
11 July 2015 Vessel 'Jenny Lee'	71°25.840' N 156°08.915' W (drift ~ 2 km/hr NW)	White floe (largely sediment-free)
14 July 2015 Vessel 'Jenny Lee'	71°25.825' N 156°14.213' W	White floe with very thick ice
	71°23.218' N 156°13.044' W (drift ~ 0.7 km/hr NW)	White floe with very thick ice
	71°23.679' N 156°15.505' W	Larger floe with thinner ice
	71°25.077' N 156°14.841' W	Uniformly thin, flat ice
13 July 2017 Vessel 'Crescent Island'	5 sites bounded within 71° 29.925' N - 71° 30.457' N and 156°09.172' W - 156°11.333' W	Uniformly thin, flat ice
17 July 2017 Vessel 'Doctor Island'	71°31.505' N 156°01.709' W	Uniformly thin, flat ice

529

530



531 Author Contribution

532 Research concept and general research plan contributed by KJ, BL, MO. BL, KJ, MO, CF, and SC designed the study and
533 planned the fieldwork. BL, MO, KJ, SC, and CF conducted the fieldwork in 2015; BL, KJ, and SF conducted the fieldwork in
534 2017. CF compiled and analyzed all field data. BL collected and analyzed all optical data. CF performed the microscopy and SF
535 analyzed the microstructure images. CF performed micro-CT measurements, and the micro-CT analyses were designed and
536 conducted by CF, SF, RL, and ZC. CF and BL prepared the manuscript with contributions from all co-authors.

537 Competing Interests

538 The authors declare no conflicts of interest.

539 Acknowledgements

540 This work was supported by NSF Award PLR-1304228 to KJ (lead PI), BL, MO. SF had additional support from a Mary Gates
541 Research Scholarship (UW). We thank Julianne Yip for help with sample collection and processing, Hannah DeLapp for data
542 organization, and Michael Hernandez for GIS help. The field campaign was successful as a result of the enterprising support of
543 the Uqpeagvik Inupiat Corporation Science staff and affiliates in Utqiagvik. Logistical support was provided by CH2M Hill Polar
544 Services.

545 References

- 546 Barber, D. G., Galley, R., Asplin, M. G., De Abreu, R., Warner, K. A., Pučko, M., Gupta, M., Prinsenberg, S., and Julien, S.:
547 Perennial pack ice in the southern beaufort sea was not as it appeared in the summer of 2009, *Geophys. Res. Lett.*, 36(24), 1–
548 5, doi:10.1029/2009GL041434, 2009.
- 549 Cox, G. F. N. and Weeks, W. F.: Equations for determining the gas and brine volumes in sea-ice samples, *J. Glaciol.*, 29(102),
550 306–316, 1983.
- 551 Crabeck, O., Galley, R. J., Delille, B., Else, B. G. T., Geilfus, N.-X., Lemes, M., Des Roches, M., Francus, P., Tison, J.-L., and
552 Rysgaard, S.: Imaging air volume fraction in sea ice using non-destructive X-ray tomography, *Cryosph.*, 10(3), 1125–1145,
553 doi:10.5194/tc-10-1125-2016, 2016.
- 554 DeAbreu, R., Yackel, J., Barber, D., and Arkette, M.: Operational Satellite Sensing of Arctic First-Year Sea Ice Melt, *Can. J.*
555 *Remote Sens.*, 27, 487–501, 2001.
- 556 Eicken, H.: Automated ice mass balance site (SIZONET), doi:10.18739/A2D08X, 2016.
- 557 Eicken, H., Krouse, H. R., Kadko, D., and Perovich, D. K.: Tracer studies of pathways and rates of meltwater transport through
558 Arctic summer sea ice, *J. Geophys. Res.*, 107(C10), 8046, doi:10.1029/2000JC000583, 2002.
- 559 Freitag, J.: The hydraulic properties of Arctic sea-ice -- Implications for the small scale particle transport (in German), *Ber.*
560 *Polarforsch.*, 325, 150 pp, 1999.
- 561 Fritsen, C. H., Lytle, V. I., Ackley, S. F., and Sullivan, C. W.: Autumn bloom of Antarctic pack-ice algae, *Science*, 266(5186),
562 782–784, 1994.
- 563 Golden, K. M., Eicken, H., Heaton, A. L., Miner, J., Pringle, D. J., and Zhu, J.: Thermal evolution of permeability and
564 microstructure in sea ice, *Geophys. Res. Lett.*, 34(16), doi:10.1029/2007GL030447, 2007.
- 565 Heggli, M., Frei, E., and Schneebeli, M.: Snow replica method for three-dimensional X-ray microtomographic imaging, *J. Glac.*,



- 566 55(192), 631–639, 2009.
- 567 Hudier, E. J. J., Ingram, R. G., and Shirasawa, K.: Upward flushing of sea water through first year ice, *Atmos. - Ocean*, 33(3),
568 569–580, doi:10.1080/07055900.1995.9649545, 1995.
- 569 Jardon, F. P., Vivier, F., Vancoppenolle, M., Lourenço, A., Bouruet-Aubertot, P., and Cuypers, Y.: Full-depth desalination of
570 warm sea ice, *J. Geophys. Res. Ocean.*, 118(1), 435–447, doi:10.1029/2012JC007962, 2013.
- 571 Jones, K. A., Ingham, M., and Eicken, H.: Modeling the anisotropic brine microstructure in first-year Arctic sea ice, *J. Geophys.*
572 *Res. Ocean.*, 117(2), 1–14, doi:10.1029/2011JC007607, 2012.
- 573 Krembs, C., Gradinger, R., and Spindler, M.: Implications of brine channel geometry and surface area for the interaction of
574 sympagic organisms in Arctic sea ice, *J. Exp. Mar. Bio. Ecol.*, 243(1), 55–80, doi:10.1016/S0022-0981(99)00111-2, 2000.
- 575 Lieb-Lappen, R. M., Golden, E. J., and Obbard, R. W.: Metrics for interpreting the microstructure of sea ice using X-ray micro-
576 computed tomography, *Cold Reg. Sci. Technol.*, 138, 24–35, doi:10.1016/j.coldregions.2017.03.001, 2017.
- 577 Light, B., Maykut, G. A., and Grenfell, T. C.: Effects of temperature on the microstructure of first-year Arctic sea ice, *J. Geophys.*
578 *Res.*, 108(C2), 3051, doi:10.1029/2001JC000887, 2003.
- 579 Light, B., Maykut, G. A., and Grenfell, T. C.: A temperature-dependent, structural-optical model of first-year sea ice, *J. Geophys.*
580 *Res.*, 109(C6), C06013, doi:10.1029/2003JC002164, 2004.
- 581 Light, B., Perovich, D. K., Webster, M. A., Polashenski, C., and Dadic, R.: Optical properties of melting first-year Arctic sea ice,
582 *J. Geophys. Res. Ocean.*, 120, doi:10.1002/2015JC011163, 2015.
- 583 Lytle, V. I. and Ackley, S. F.: Heat flux through sea ice in the western Weddell Sea: Convective and conductive transfer
584 processes *J. Geophys. Res.*, 101(C4), 8853–8868, doi:10.1029/95JC03675, 1996.
- 585 Nansen, F.: *Farthest North*, Vol 1, Archibald Constable and Company, Westminster, 510 pp, 1897.
- 586 Perovich, D. K. and Gow, A. J.: A quantitative description of sea ice inclusions, *J. Geophys. Res.*, 101(C8), 18327,
587 doi:10.1029/96JC01688, 1996.
- 588 Perovich, D. K., Grenfell, T. C., Light, B., and Hobbs, P. V.: Seasonal evolution of the albedo of multiyear Arctic sea ice, *J.*
589 *Geophys. Res.*, 107(C10), 8044, doi:10.1029/2000JC000438, 2002.
- 590 Pringle, D. J., Miner, J. E., Eicken, H., and Golden, K. M.: Pore space percolation in sea ice single crystals, *J. Geophys. Res.*
591 *Ocean.*, 114(12), 1–14, doi:10.1029/2008JC005145, 2009.
- 592 Richter-Menge, J. A., and Jones, K. F.: The tensile strength of first-year sea ice, *J. Glaciol.*, 39(133), 609–618, 1993.
- 593 Soille, P.: On the morphological processing of objects with varying local contrast, in *Discrete geometry for computer imagery*,
594 *Proceedings*, edited by I. Nystrom, G. S. DiBaja, and S. Svensson, Springer-Verlag, Berlin, pp. 52–61, doi:10.1007/b94107,
595 2003.
- 596 Stroeve, J. C., Markus, T., Boisvert, L., Miller, J., and Barrett, A.: Changes in Arctic melt season and implications for sea ice loss,
597 *Geophys. Res. Lett.*, 41(4), 1216–1225, doi:10.1002/2013GL058951, 2014.
- 598 Timco, G. and Johnston, M.: Ice Strength During the Melt Season, in *Proceedings of the 16th IAHR International Symposium on*
599 *Ice*. v. 2, edited by V. Squire and P. Langhorne, Univ. of Otago, Dunedin, 2002.
- 600 Timco, G. W. and O'Brien, S.: Flexural strength equation for sea ice, *Cold Reg. Sci. Technol.*, 22(3), 285–298, doi:10.1016/0165-



- 601 232X(94)90006-X, 1994.
- 602 Untersteiner, N.: Natural desalination and equilibrium salinity profile of perennial sea ice, *J. Geophys. Res.*, 73(4), 1251–1257,
603 doi:10.1029/JB073i004p01251, 1968.
- 604 Vancoppenolle, M., Bitz, C. M., and Fichefet, T.: Summer landfast sea ice desalination at Point Barrow, Alaska: Modeling and
605 observations, *J. Geophys. Res. Ocean.*, 112(4), 1–20, doi:10.1029/2006JC003493, 2007.
- 606 Weeks, W. F.: On the history of research on sea ice, in *Physics of ice-covered seas, vol. 1*, edited by M. Leppäranta, pp. 1–24,
607 University of Helsinki, Helsinki, Finland, 1998.
- 608 Weeks, W. F. and Ackley, S. F.: The growth, structure, and properties of sea ice, in *The Geophysics of Sea Ice*, edited by N.
609 Untersteiner, pp. 9–164, Plenum Press, New York, 1986.
- 610 Wettlaufer, J. S., Worster, M. G., and Huppert, H. E.: Solidification of leads: Theory, experiment, and field observations, *J.*
611 *Geophys. Res.*, 105(C1), 1123, doi:10.1029/1999JC900269, 2000.
- 612 Zhou, J., Delille, B., Eicken, H., Vancoppenolle, M., Brabant, F., Carnat, G., Geilfus, N.-X., Papakyriakou, T., Heinesch, B., and
613 Tison, J.-L.: Physical and biogeochemical properties in landfast sea ice (Barrow, Alaska): Insights on brine and gas
614 dynamics across seasons, *J. Geophys. Res. Ocean.*, 118(6), 3172–3189, doi:10.1002/jgrc.20232, 2013.